

2.4 Electronic properties of systems with reduced dimensions

(Following J.H. Davies “The Physics of low-dimensional semiconductors”, Cambridge University Press, Cambridge, UK (1998), and lecture notes by D.A. Wharam)

Recap:

→ See Introduction (ch. 1.2(ii), Density of states in reduced dimensions: Electrons)

Consider a system of N non-interacting electrons (fermions with spin $= \pm \frac{1}{2}\hbar$, i.e. each allowed \vec{k} -state in the discretized k-space can accommodate up to two electrons). The electronic density for the number N of occupied states in the Fermi sphere at $T = 0$ K up to the Fermi wave-vector k_F is given by:

$$n = \frac{N}{V} = \frac{2 \frac{4}{3} \pi k_F^3}{\frac{8\pi^3}{V} V} = \frac{k_F^3}{3\pi^2} \quad (2.49)$$

The **density of states** (DOS) is an important measure of the number of states which are available for occupancy, or more generally at the Fermi energy, for transport processes. By definition,

$$g(\epsilon) = \frac{1}{V} \frac{\partial N}{\partial \epsilon} = \frac{\partial n}{\partial \epsilon} \quad (2.50)$$

The dimensionality plays a significant role when considering the properties of nanostructures, which are invariably systems of reduced dimensionality. The following dependencies of the DOS on the energy are found (with m the effective mass):

$$\mathbf{3D:} \quad g_{3D}(\epsilon) = \frac{\partial n}{\partial \epsilon} = \frac{\sqrt{2\epsilon m^3}}{\pi^2 \hbar^3} = c_{3D} \sqrt{\epsilon}$$

$$\mathbf{2D:} \quad g_{2D}(\epsilon) = \frac{1}{A} \frac{\partial N}{\partial \epsilon} = \frac{m}{\pi \hbar^2} = c_{2D}$$

$$\mathbf{1D:} \quad g_{1D}(\epsilon) = \frac{1}{L} \frac{\partial N}{\partial \epsilon} = \frac{1}{\pi \hbar} \sqrt{\frac{2m}{\epsilon}} = \frac{c_{1D}}{\sqrt{\epsilon}}$$

$$\mathbf{0D:} \quad g_{0D}(\epsilon) = \delta(\epsilon)$$

Thus the 3D density of states scales with $\sqrt{\epsilon}$, the 2D density of states is constant, the 1D density of states is proportional to $1/\sqrt{\epsilon}$, and the 0D density of states is a series of discrete delta-functions. Note that the existence of excited states (occupation of more than one state) leads to the formation of subbands, see Fig. 2.26.

In general:

- Volume of a d -dimensional sphere: $V_d = \gamma_d R^d$ with γ_d : $\gamma_1 = 2$, $\gamma_2 = \pi$, $\gamma_3 = \frac{4}{3}\pi$
- Number of states in k-space with a wave vector $\leq k$: $N = \frac{2V_k}{(2\pi)^d} V = \frac{2\gamma_d k^d}{(2\pi)^d} L^d$
- Electron density: $n = N/V = \frac{2\gamma_d k^d}{(2\pi)^d}$
- $\epsilon = \frac{\hbar^2 k^2}{2m}$ thus $k = \frac{1}{\hbar} \sqrt{2m\epsilon}$
- $g(\epsilon) = \frac{\partial n}{\partial \epsilon} = \frac{d\gamma_d (2m)^{d/2}}{(2\pi\hbar)^d} \epsilon^{\frac{d}{2}-1}$

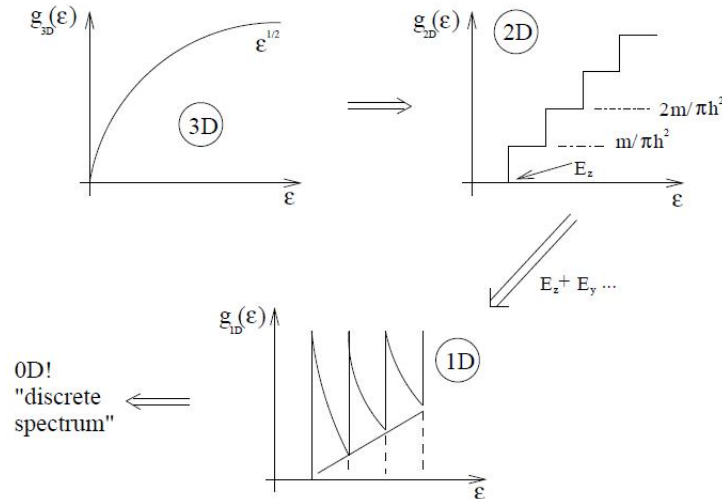
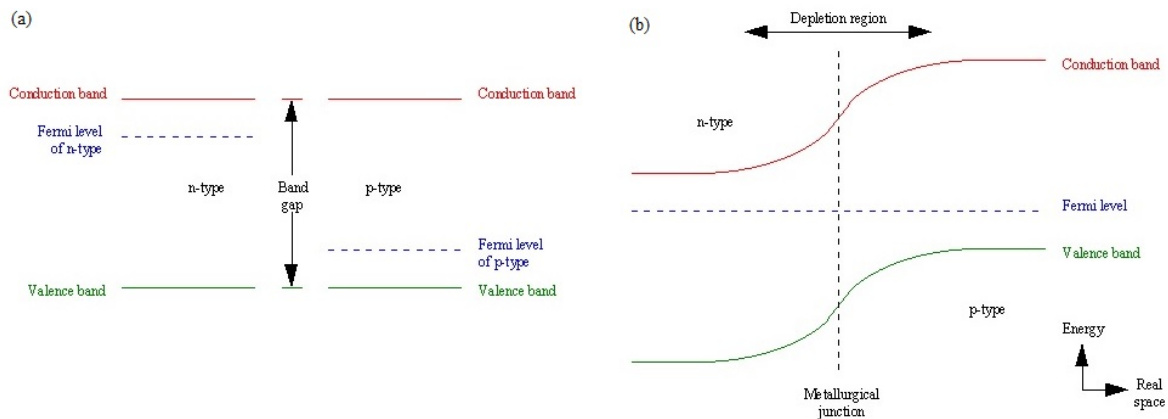


Fig. 2.26: Density of states in 3D, (quasi-)2D, (quasi-)1D and quasi-0D

2.4.1 (Quasi-)2dim quantization in heterostructures

Fig. 2.27: Band structure of the two materials in a homojunction (a) before contact, (b) in contact [<http://www.liv.ac.uk/renewable-energy/about/staff/ken-durose/>]

Homojunction: Interface between two semiconductors that have identical bandgaps, but may have different properties such as doping (Figure 2.27).

Heterojunction: Interface between two semiconductors with different bandgaps.

Semiconductors are characterized by the following energies:

- Band edge energies (ϵ_V for valence band, ϵ_C for conductance band)
- Band gap E_g
- Chemical potential μ or Fermi energy ϵ_F
- Electron affinity χ (surface property)
- Work function $q\Phi_m$ (surface property)

Consider the heterojunction formed between two different bulk semiconductors in contact (Figure 2.28). Bringing the two materials into contact leads to the defini-

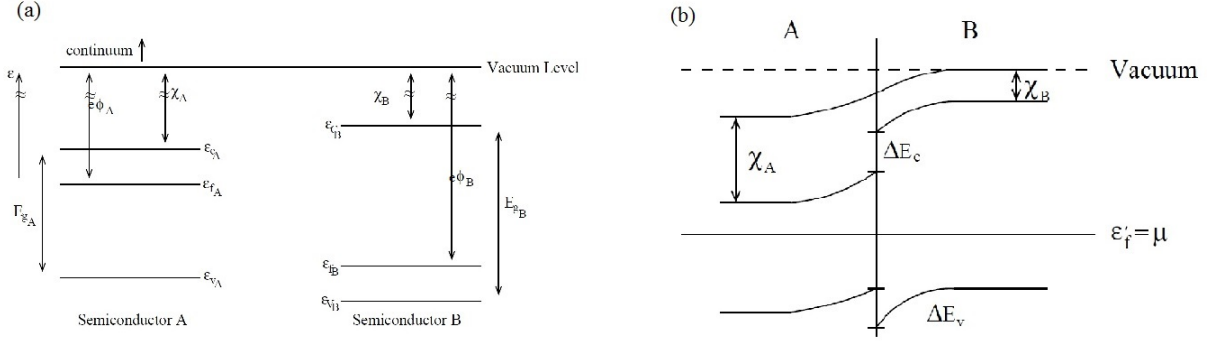


Fig. 2.28: (a) Sample band structure of a heterostructure before contact; (b) position dependent band bending and band discontinuity in a heterojunction

tion of a well-defined electrochemical potential throughout the whole material, i.e. $\epsilon'_{F_A} = \epsilon'_{F_B} = \mu \forall \vec{r}$ in the material. As for a standard pn-homojunction, the following effects will occur in the equilibrium state due to a redistribution of charge carriers:

- depletion regions
- band-bending
- creation of a built-in potential $\Phi_{bi}(\vec{r})$.

The resulting position-dependent bandstructure then takes the general form shown in Figure 2.28(b). In contrast to homojunctions, heterojunctions additionally exhibit **band edge discontinuities** ($\Delta\epsilon_c$ and $\Delta\epsilon_v$), which are of crucial significance for device physics and can be influenced by **bandgap engineering**.

Example: Creation of a 2dim electron gas at a heterojunction interface: Donor doping in a material with a large band gap brought into contact with a neutral (or weakly p-type) material of a smaller band gap can lead to the creation of a degenerate electron gas at the heterojunction interface. The most widely used example of this technique is the GaAs-AlGaAs system, where the tertiary alloy is characterised by the fraction of aluminum atoms, i.e. $Al_xGa_{(1-x)}As$, with typically $x \simeq 0.3$.

Material	$Al_xGa_{(1-x)}As$	$GaAs$
-	n-doped (Si) 10^{18} cm^{-3}	p-type, weak or undoped, 10^{15} cm^{-3}
Band gap	$E_g \simeq 1.42 - 2.16 \text{ eV}$	$E_g \simeq 1.42 \text{ eV}$

This combination yields the “self-consistent” conductance band structure shown in Figure 2.29. It thus leads to the creation of a roughly triangular quantum well at the heterojunction interface. By careful tuning of the energies involved, one can engineer the band structure such that only the first discrete energy level within the quantum well lies below the Fermi energy. At low temperatures, only states in the first energy level E_1 are occupied and a **two-dimensional electron gas** is created.

In order to get some insight into the details of this configuration, the thermodynamic problem taking into account both the electrostatics (Poisson equation) and the quantum mechanics (Schrödinger equation) of the triangular potential well can be solved. For a triangular quantum well, the lowest quantised state can be related to the field

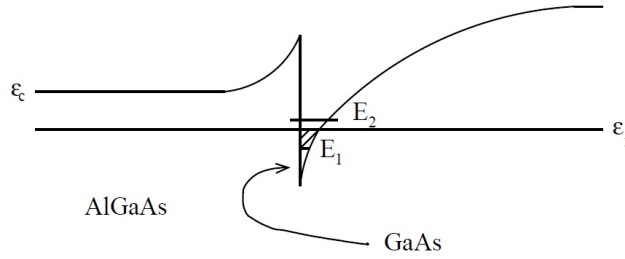


Fig. 2.29: Creation of a triangular quantum well in an AlGaAs-GaAs heterostructure

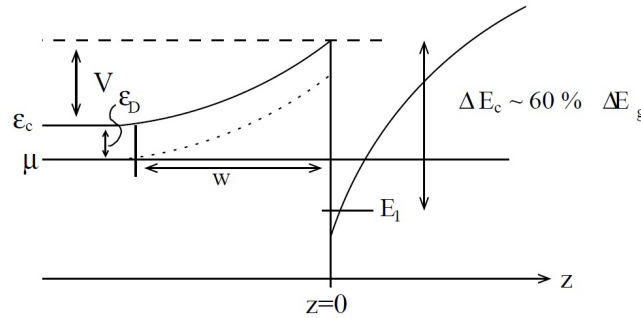


Fig. 2.30: Relevant parameters of the approximately triangular potential well

strength F at the interface via

$$E_1 = \left(\frac{\hbar^2}{2m^*} \right)^{1/3} \left(\frac{9\pi e F}{8} \right)^{2/3} \quad (2.51)$$

(cf. chapter Field Effect Transistor), and hence via Gauss to the surface density of electrons N_S at, or rather in the vicinity of, the interface where the band bending occurs. The relevant parameters are indicated in Fig. 2.30.

$$F = \frac{N_S e}{\epsilon_0 \epsilon_r} \quad (2.52)$$

Inserting F , the lowest energy state can directly be related to the 2D density N_S :

$$E_1 = \left(\frac{\hbar^2}{2m^*} \right)^{1/3} \left(\frac{9\pi e^2 N_S}{8\epsilon_0 \epsilon_r} \right)^{2/3} = \text{const.} * N_S^{2/3} \quad (2.53)$$

For a two-dimensional system the density is also implicitly related to the Fermi energy and wave vector, thus:

$$E_F = E_1 + \frac{\hbar^2 k_F^2}{2m^*} = E_1 + \frac{\pi \hbar^2}{m^*} N_S \quad (2.54)$$

using $k_F^2 = 2\pi N_S(2D)(= k_x^2 + k_y^2)$; $k_F^3 = 3\pi^2 N_V(3D)$.

Under the assumption of a constant dopant density N_d in the AlGaAs material and the condition for charge neutrality $N_d w = N_S$ (assuming that the excess electrons of the

surface electron density N_s result from redistributing electrons with the bulk density N_d across the depletion length w of the band bending region), we can calculate the depletion potential by integration:

$$V_{dep} = - \int_0^{-w} F dz = \int_0^{-w} \frac{eN_d z}{\epsilon_0 \epsilon_r} dz = \frac{eN_d w^2}{2\epsilon_0 \epsilon_r} \quad (2.55)$$

From the above, the band edge discontinuity ΔE_C can be calculated to

$$\Delta E_C = E_1(N_s) + \frac{\pi \hbar^2 N_s}{m^*} + \epsilon_D + eV_{dep} \quad (2.56)$$

with ϵ_D the energy spacing between the Fermi level and ϵ_C . Once ΔE_C is determined, the above can be used as a method for computing the two-dimensional density:

$$\Delta E_C - \frac{e^2 N_s^2}{2\epsilon_r \epsilon_0 N_d} - \epsilon_D = E_1(N_s) + N_s \frac{\pi \hbar^2}{m^*} \quad (2.57)$$

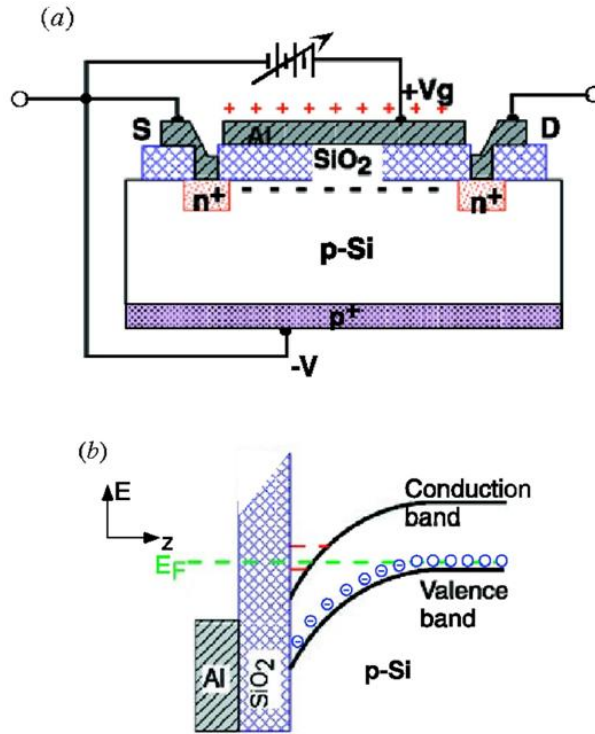


Fig. 2.31: Realization of a two-dimensional electron gas in a silicon MOSFET

Figure 2.31 schematically shows the realization of a two-dimensional electron gas in a Metal-Oxide-Semiconductor Field Effect Transistor (MOSFET). Figure 2.32 outlines the geometry of a GaAs/AlGaAs heterostructure including a two-dimensional electron gas. State-of-the-art two-dimensional electron gases in GaAs/AlGaAs at temperatures < 1 K can exhibit ultra-high electron mobilities up to $> 10^7$ cm²/(Vs)!

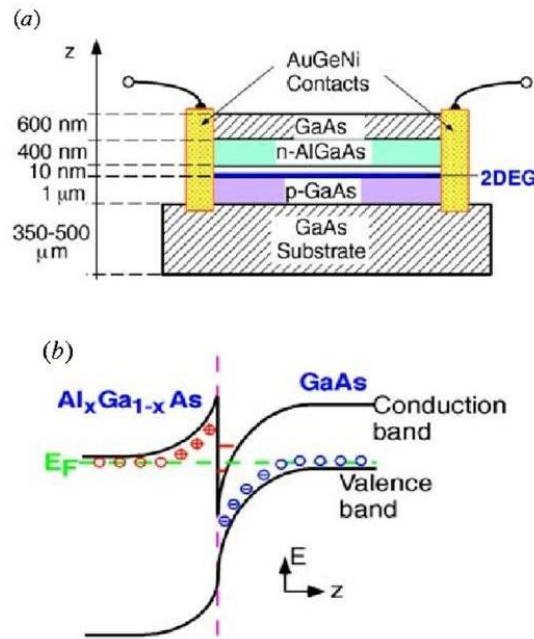


Fig. 2.32: Realization of a 2D electron gas in a GaAs/AlGaAs heterostructure

The experimental realisation of a GaAs/AlGaAs sample for low-temperature transport measurements is sketched in Figs. 2.33 and 2.34. The layer system is grown by molecular beam epitaxy with single atomic layer precision. A superlattice buffer of ultra-thin alternating GaAs and AlGaAs layers is grown to create an atomically flat surface on top of a GaAs substrate by making use of the strain induced by the slightly different lattice spacings. The 2D electron gas is created at the interface between the following GaAs and AlGaAs layers. A silicon doped AlGaAs layer is introduced to supply additional electrons to the 2D electron gas, but is separated from the interface by an undoped layer to reduce impurity scattering. The top layers are added to avoid oxidation. The conductance band edge corresponding to this layer structure is shown in Fig. 2.33 (left) and exhibits a triangular quantum well below the Fermi energy at the location of the 2D electron gas, where locally a high electron density is observed. Fig. 2.34 schematically outlines the steps for fabricating a sample with a buried 2D electron gas contacted by electrodes using optical lithography. A photoresist layer is spin-coated onto the GaAs/AlGaAs substrate with the buried 2D electron gas. The resist is structured through a mask by optical lithography, and a mesa structure is defined after wet-chemical development. The mesa structure is transferred into the substrate by etching until the 2D electron gas outside the mesa structure is removed. After removal of the residual resist, the final mesa structure is defined in the substrate. This Hall bar is contacted by repeating the optical lithography steps (second mask level) to define metallic contacts, which are annealed at several 100 °C to contact the buried electron gas with ohmic current-voltage-characteristics. The ohmic contacts are covered by larger metallic bond pads in the next optical lithography steps (third mask level) which are used for attaching thin metallic wires by wire bonding. The other side of the wires is attached to a chip carrier. By contacting the chip carrier, low currents can be applied to the structure, and the longitudinal and transversal voltages can be measured in a four-point configuration.

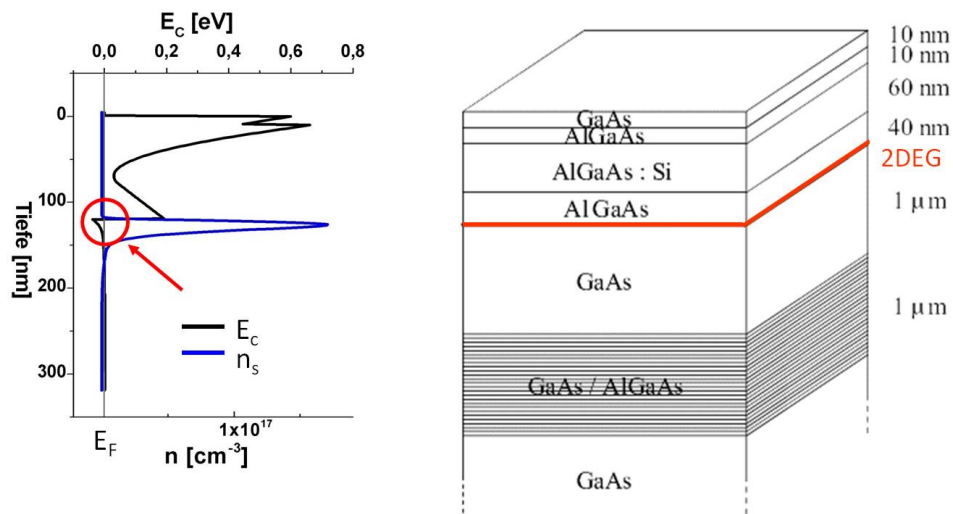


Fig. 2.33: Epitaxial layer system of a GaAs/AlGaAs sample with a 2D electron gas with corresponding conductance band structure E_c and (quasi-)free electron density n_s

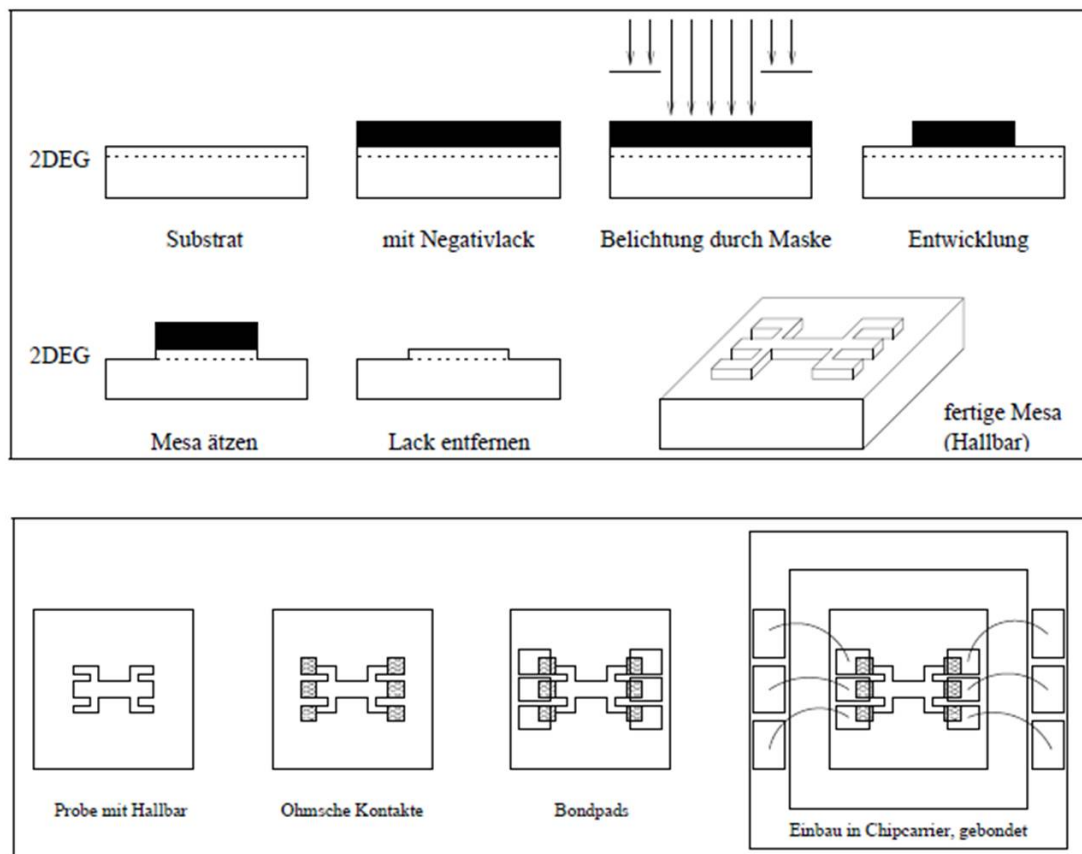


Fig. 2.34: Schematic fabrication steps of a "mesa" (Hall bar) structure for transport measurements in a 2D electron gas

2.4.2 Conductance in low-dimensional systems

The Boltzmann conductivity may be derived by considering the motion of an electron under the influence of an external force $\vec{f}(t)$ and the assumption of a relaxation time τ (mean time between collisions) in which the momentum of an electronic state is randomised. The electronic velocity \vec{v} , or equally the momentum \vec{p} , can readily be related to the current density \vec{j} carried by an ensemble of such electrons in the material:

$$\vec{j} = -ne\vec{v} = -\frac{ne\vec{p}}{m^*} \quad (2.58)$$

where n is the density of valence electrons and m^* the effective mass. In the relaxation time approximation the evolution of the momentum as a function of time can be obtained by considering how such an electron evolves under the external field. Neglecting second order corrections, one gets a differential equation for the momentum $\vec{p}(t)$:

$$\frac{d\vec{p}}{dt} = -\frac{\vec{p}(t)}{\tau} + \vec{f}(t) \quad (2.59)$$

This expression can be applied to many cases of practical interest. Considering the simple case $\vec{f}(t) = -e\vec{E}$, the average momentum per carrier is expected to be independent of time, leading to

$$\frac{d\vec{p}}{dt} = -\frac{\langle \vec{p} \rangle}{\tau} - e\vec{E} = 0 \quad (2.60)$$

Thus $\langle \vec{j} \rangle = \frac{ne^2\tau}{m^*}\vec{E}$. This microscopic version of Ohm's law relates the local current density to the field strength, and the constant of proportionality $\sigma = \frac{ne^2\tau}{m^*}$ is called the **Boltzmann conductivity**. In general the effective mass m^* is a tensor, $\frac{1}{M_{ij}} = \frac{1}{\hbar^2} \frac{\partial^2 \epsilon}{\partial k_i \partial k_j}$, i.e. \vec{j} is not necessarily parallel to \vec{E} , but for isotropic crystal systems the effective mass may be taken as a scalar quantity.

The mean free time is determined by temperature-dependent scattering mechanisms. At low temperatures, few phonons are available for scattering, and impurity scattering becomes dominant.

Role of the electrons at the Fermi surface:

In a simple picture, the Fermi surface under the influence of an external field can be considered as a shifted Fermi surface in k -space, which constantly relaxes to the ground state as a result of scattering (Fig. 2.35).

For sufficiently low field strengths, the electronic transport can be regarded as a property of the electrons at the Fermi surface. With $\Delta k \ll k_F$ or $\frac{\Delta k}{k_F} \ll 1$

$$\frac{\Delta \vec{p}}{\hbar k_F} \ll 1 \quad \text{or} \quad \frac{eE\tau}{\hbar k_F} \ll 1 \quad \Rightarrow \quad E < 10^5 \text{ Vm}^{-1} \quad (2.61)$$

In low temperature experiments one generally considers **linear response properties** (limit $E \rightarrow 0$), thus the perturbations of the Fermi surface are minimal (typical experiments: 10 μV applied to 1 mm devices $\hat{=}$ 10^{-2} Vm^{-1}).

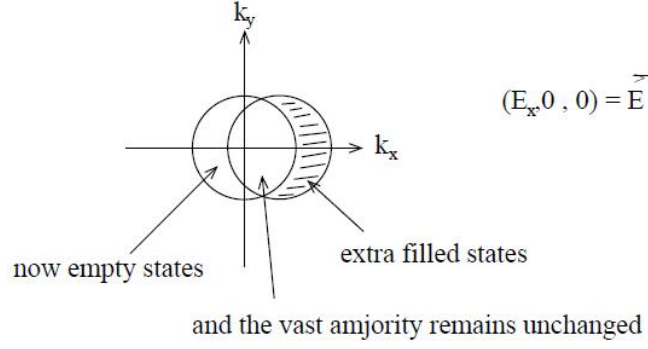


Fig. 2.35: Shift of the Fermi surface in an external field

For free electrons, $\epsilon_F = \frac{\hbar^2 k_F^2}{2m}$, and the electron density can be written as $n = \frac{k_F^d}{d(\pi^{d-1})}$, with d the dimensionality of the system and $d \in \{2, 3\}$. The density of states then is

$$g(\epsilon_F) = \frac{dn}{d\epsilon}|_{\epsilon=\epsilon_F} = \frac{2m(2m\epsilon)^{\frac{d}{2}-1}}{\hbar^d \cdot 2(\pi^{d-1})} \quad (2.62)$$

With some simple manipulations the Boltzmann conductivity can be rewritten as

$$\sigma_B = \frac{ne^2\tau}{m} = g(\epsilon_F)e^2 \cdot \frac{2\epsilon_F\tau}{md} \quad (2.63)$$

The factor $\frac{2\epsilon_F\tau}{md}$ is known as the **Einstein diffusion constant**:

$$D = \frac{2\epsilon_F\tau}{md} = \frac{v_F^2\tau}{d} \quad (2.64)$$

with the Fermi velocity $v_F = \hbar k_F/m$. This approach to electronic transport demonstrates that the conductivity may be related purely to the electrons at the Fermi surface and the diffusion constant for their motion: $\sigma_B = g(\epsilon_F)e^2D$ + quantum corrections.

Mesoscopic length scales

The **mesoscopic regime** addresses the intermediate transition region between the classical and the quantum mechanical regime, typically on a length scale of $\sim 1 \mu\text{m}$ to 100 nm , where objects start revealing quantum mechanical properties.

The **quantum corrections** observed in mesoscopic samples depend strongly on the interplay of many different length scales. In the low-temperature limit inelastic scattering mechanisms become weaker, and the dominant scattering mechanism is elastic scattering from fixed impurities (e.g. dopant atoms). The associated scattering time determines many parameters and different transport regimes.

Relevant length scales include:

- **Fermi wavelength** $\lambda_F = \frac{2\pi}{k_F}$: largely independent of dimensionality, relatively large in semiconductor systems

- **Elastic mean free path l_e :** also known as elastic scattering or momentum relaxation length; $l_e = v_F \tau_e$ with $v_F = \frac{1}{\hbar} \left(\frac{\partial \epsilon}{\partial k} \right)_{k=k_F}$, τ_e elastic scattering time
- **Inelastic scattering length $l_{in} = \sqrt{D\tau_{in}}$:** generally associated with energy relaxation and therefore phase-relaxation of the electronic wave functions
- **Phase coherence length l_Φ :** Often, but not always equal to the inelastic scattering length
- **Magnetic length $l_B = \sqrt{\frac{\hbar}{eB}}$:** a phase shift of the wave functions leads to modified interference (Aharonov Bohm effect) or a loss of coherence (weak localisation)
- **Sample size L_x, L_y, L_z :** Plays a crucial role in determining both the dimensionality of the density of states and the dimensionality of the observed phenomena.

Low-dimensional systems

By introducing **geometric restrictions**, the motion of charge carriers can be constrained in one or more dimensions through growth techniques and/or surface properties, as well as lateral structuring by electron beam lithography. The density of states is modified. By performing low-temperature measurements, it is possible to only populate the lowest available states in k-space in any given dimension(s).

As a consequence, a **2-dimensional electron gas** can be created. Quantisation into **Landau levels** appears when sufficiently high magnetic fields are applied, leading to the appearance of the **quantum Hall effect** in 2-dimensional systems. In **(quasi-)1-dimensional quantum wires or quantum point contacts**, **conductance quantisation** is observed in the transport properties of the wire. In **(quasi-)0-dimensional quantum dots**, their discrete energy level systems lead to **Coulomb blockade** and the observation of **charge quantisation** in the transport.

In the following the different quantisation mechanisms will be examined more closely.

2.4.3 Low-dimensional systems in high magnetic fields

Landau quantisation

When sufficiently high magnetic fields are applied to low-dimensional systems, the Lorentz force starts to play a relevant role. **Landau quantisation** is observed in the plane perpendicular to the applied magnetic field, while the classical motion in the direction of the magnetic field remains unaffected.

Landau quantisation can be derived by taking into account the magnetic field via the magnetic vector potential in Schrödinger's equation using the momentum $\vec{p} \rightarrow \vec{p} - e\vec{A}$, the momentum operator $\hat{p} = -i\hbar\nabla$, and the Landau gauge $\vec{A} = (0, Bx, 0)$ for $\vec{B} = (0, 0, B)$. Then

$$H\psi = \frac{1}{2m}(\vec{p} - e\vec{A})^2\psi = \frac{1}{2m}(p_x^2 + (p_y - eBx)^2 + p_z^2)\psi = E\psi \quad (2.65)$$

Both p_y and p_z commute with the Hamiltonian $[H, p_y] = [H, p_z] = 0$, therefore solutions with simultaneous eigenfunctions of p_y, p_z and H can be constructed:

$$\psi(\vec{r}) = \phi(x)\exp[ik_y y]\exp[ik_z z] \quad (2.66)$$

Inserting this solution in the above equation yields

$$\frac{1}{2m}\left(-\hbar^2\frac{d^2}{dx^2} + e^2B^2\left(x - \frac{\hbar k_y}{eB}\right)^2\right)\phi(x) = \left(\epsilon - \frac{\hbar^2 k_z^2}{2m}\right)\phi(x) = \epsilon'\phi(x) \quad (2.67)$$

The equation corresponds to that of a simple harmonic oscillator with the following properties and corrections:

- Energy correction $\epsilon \rightarrow \epsilon - \frac{\hbar^2 k_z^2}{2m}$ originating from the motion parallel to the magnetic field
- Coordinate shift $x \rightarrow x - \frac{\hbar k_y}{eB}$ where the quantum number k_y localises the electrons within the sample.
- Solutions: $\phi_n(x) = \left(\frac{eB}{\pi\hbar}\right)^{1/4} \frac{1}{2^{n/2}\sqrt{n!}} \exp\left(\frac{-eBx^2}{2\hbar}\right) H_n\left(\left(x - \frac{\hbar k_y}{eB}\right)\sqrt{\frac{eB}{\hbar}}\right)$, with H_n the Hermite polynoms.
- Energies of the solution: $E(n, k_z) = \hbar\omega_c\left(n + \frac{1}{2}\right) + \frac{\hbar^2 k_z^2}{2m}$ with $n \in \mathbb{N}$ and the cyclotron frequency $\omega_c = eB/m$.
- The solution for the motion in the x-y-plane (perpendicular to \vec{B}) is that of a simple harmonic oscillator with a confining potential of $\frac{1}{2}m\omega_c^2 x^2$.

The energy levels in the x-y-plane $E_n = (n + \frac{1}{2})\hbar\omega_c$ are known as **Landau levels**. The degeneracy of the Landau levels, i.e. the number of states per level, can be calculated by taking into account the boundary condition in the y-direction $\psi(y) = \psi(y + L_y)$ with the requirement $k_y L_y = 2\pi n$ with $n \in \mathbb{N}$. Also by requiring that the electrons are localized within the sample ($0 < x < L_x$), the following criterion holds for n :

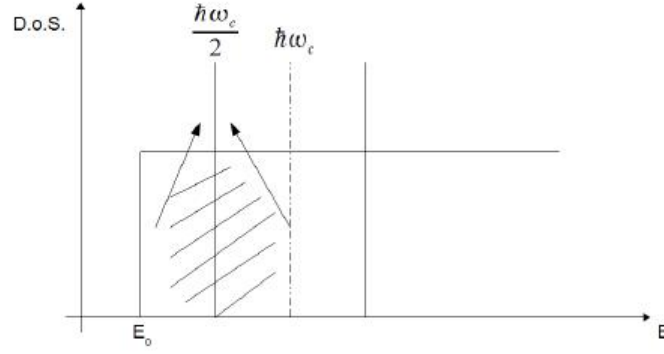


Fig. 2.36: Energy-dependent 2D density of states without and with a magnetic field applied

$$0 \leq \frac{\hbar k_y}{eB} \leq L_x \quad \Rightarrow \quad 0 \leq n \frac{2\pi\hbar}{eB} \leq L_x L_y \quad (2.68)$$

Thus the number of states per Landau level (without taking into account the spin degeneracy, which adds another factor of 2, and potential valley degeneracy from band-structure effects), amounts to

$$n_{max} = \frac{eB}{2\pi\hbar} L_x L_y \quad (2.69)$$

Through the formation of Landau levels, the constant 2D density of states $\frac{m}{2\pi\hbar^2}$ (i.e. $\frac{m}{\pi\hbar^2}$ including spin degeneracy) breaks up into a series of discrete energy levels at an equal spacing of $\hbar\omega_c$. For each such interval of the constant density of states, the electrons are redistributed to the respective Landau level (see Fig. 2.36), corresponding to $\frac{m}{2\pi\hbar^2} \times \hbar\omega_c = \frac{eB}{2\pi\hbar}$ without spin-/valley-degeneracy. The equidistantly spaced states in k-space at $B = 0$ are reordered to occupy circles with discrete energies, as shown in Fig. 2.37.

The energy level spacing $\hbar\omega_c = \hbar \frac{e}{m} B$ as well as the level degeneracy are directly proportional to the magnetic field strength B . Thus by increasing the magnetic field, the higher energy Landau levels are subsequently depleted when crossing the Fermi energy, while the electrons are redistributed to the lower lying Landau levels accomodating an increasing number of electronic states each. This simplified picture is visualized in the Landau fan of states, Fig. 2.38. The number of occupied Landau levels (including the uppermost partially occupied level) in dependence of the magnetic field is described by the **filling factor**

$$\nu = \frac{n_{2D}}{eB/2\pi\hbar} = \frac{n_{2D}\hbar}{eB} \quad (2.70)$$

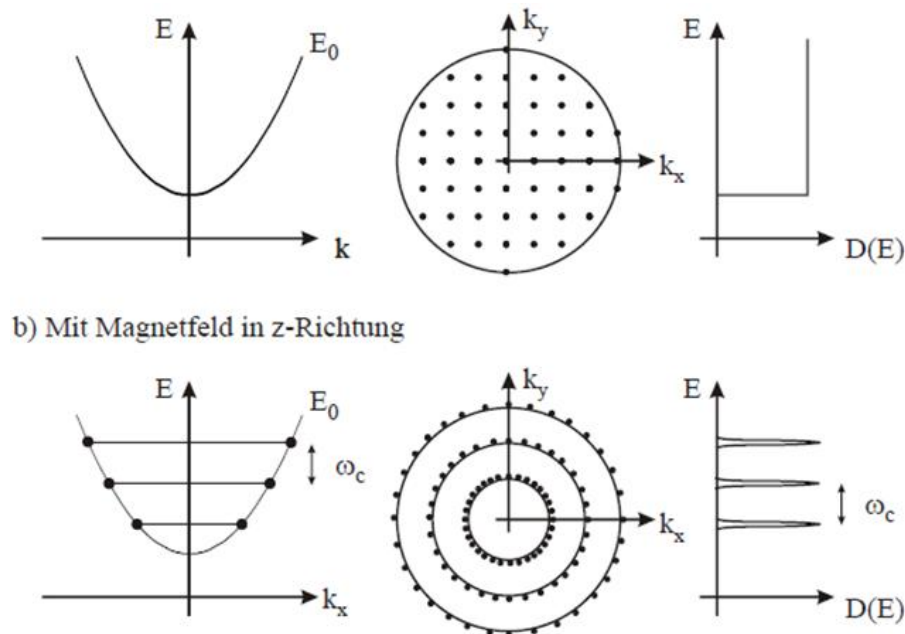


Fig. 2.37: a) Without an external magnetic field, the states are distributed on the lowest energy subband. In k -space they are equidistantly spaced within the Fermi sphere of radius k_F . The density of states of the first 2D subband is constant with energy. b) When an external B -field is applied, Landau quantisation takes place. Only states within the subbands at discrete energy values E_n are occupied. In k -space the states are forced onto spherical orbits. The density of states splits up into discrete levels [T. Klar, Praktikumsanleitung Universität Giessen]

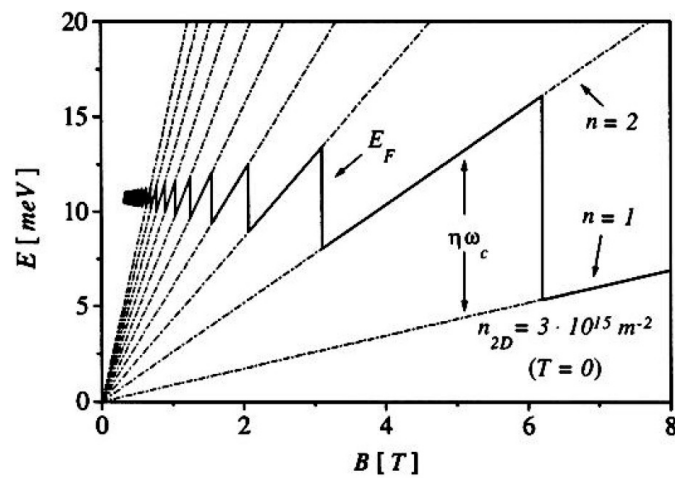


Fig. 2.38: Landau fan: development of 2D density of states in a magnetic field [J. Lohse, Dissertation Universität Hamburg, 2003]

Shubnikov-de Haas effect

A frequently observed effect for 2D systems in high magnetic fields with low temperatures is the Shubnikov-de Haas effect. The longitudinal resistance ρ_l or conductance $\sigma_l = (\rho_l)^{-1}$ exhibits oscillations in a quantizing field that fulfils the conditions $\omega_c \tau > 1$, i.e. several cyclotron orbits can be completed, and $\hbar\omega_c > k_B T$, i.e. the thermal broadening is small compared to the separation of the Landau levels. The oscillation period of the conduction electrons changes proportionally to changes in the magnetic field strength, such that the oscillation minima are spaced at a constant value of $\Delta(1/B)$. The Shubnikov-de Haas oscillations can be used to estimate the carrier concentration to $n_e \simeq \frac{e}{h} \frac{1}{\Delta(1/B)}$. According to [Ando et al., Rev. Mod. Phys. 54, 437 (1982), and Adams & Holstein, J. Phys. Chem. Sol. 10, 254 (1959)], the longitudinal conductance shows a \cos dependence (Fig. 2.39).

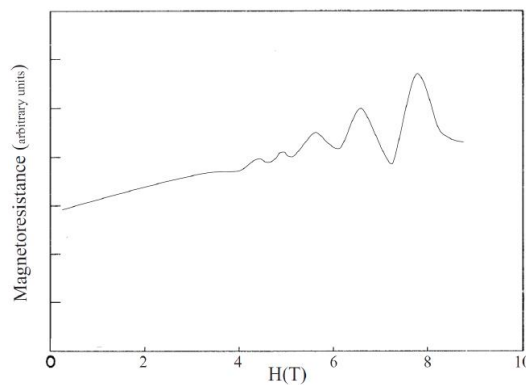


Fig. 2.39: Shubnikov-de Haas oscillations

Quantum Hall Effect

The quantum Hall effect at high magnetic fields manifests itself in four-point measurements (see Fig. 2.40) of two-dimensional electron gases by the simultaneous occurrence of nearly zero resistance ρ_l in the longitudinal resistance and highly constant plateaus ρ_H in the transversal resistance, independent of the material system or the sample geometry:

$$\rho_l \simeq 0 - 10^{-10} \Omega/\square \quad (2.71)$$

which is a factor of about 1000 smaller than the area resistance in any other non-superconducting system, and

$$\rho_H = \frac{h}{e^2} \frac{1}{n} = \frac{1}{n} 25812.807 \Omega \quad \text{with } n \in \mathbb{N} \quad (2.72)$$

with a precision of the Hall resistance within the plateaus of better than 10^{-7} .

The quantum Hall effect was first observed by K. von Klitzing et al. in 1980 (Fig. 2.41), which was rewarded by the Nobel Prize in physics already in the year 1985. The constant resistance value of $25\,812.807 \Omega$ has been defined as the **von Klitzing constant** R_K , which was introduced as the new international standard for resistance measurements in 1990.

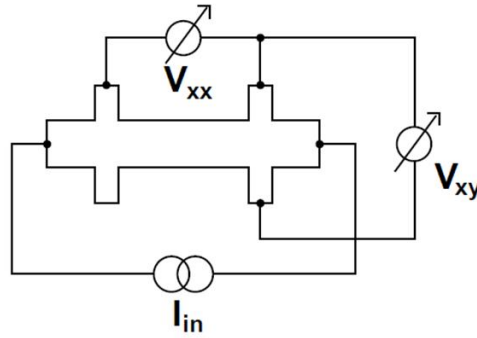


Fig. 2.40: 4-point configuration for the measurement of the longitudinal resistance ρ_l via the voltage V_{xx} and the transversal resistance ρ_H via the voltage V_{xy}

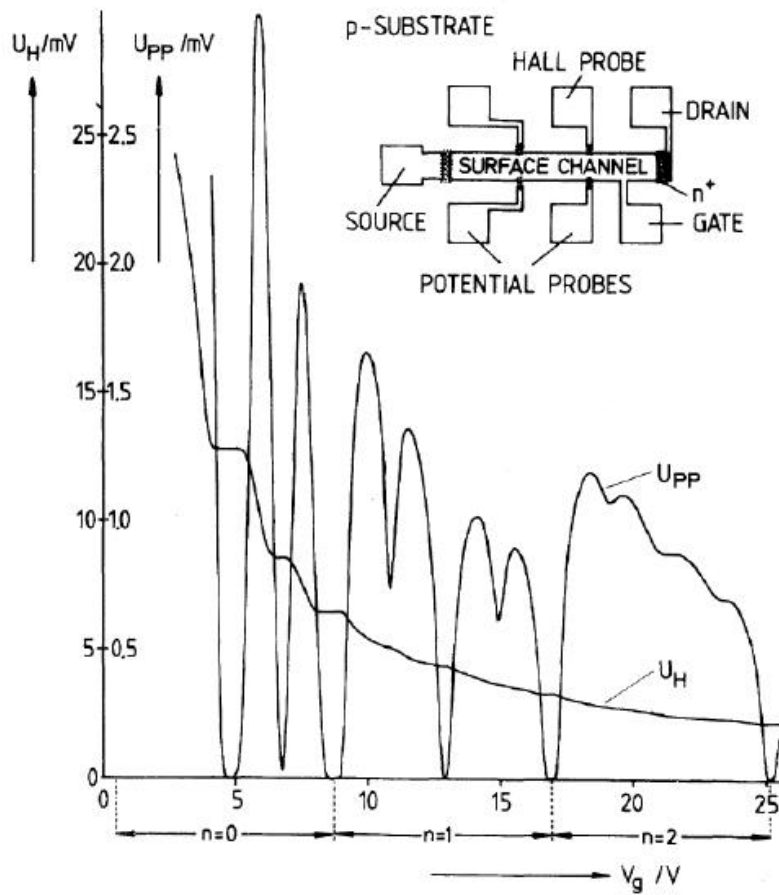


Fig. 2.41: Longitudinal and Hall voltage in the quantum Hall effect [K. von Klitzing et al., Phys. Rev. Lett. 45, 494 (1980)] at $T = 1.5$ K, $I = 1 \mu\text{A}$, $B = 18$ T

Qualitatively these observations can be explained by the appearance of edge channels in the Hall samples. Landau levels are accompanied by cyclotron orbits of electrons in the 2D electron gas, which do not contribute to the current through the sample when the Fermi energy is located between Landau levels, where no electronic states are present at the Fermi energy (see Fig. 2.42). At the sample edge however, the level energies are modified by the confining potential, and cross the Fermi energy at defined

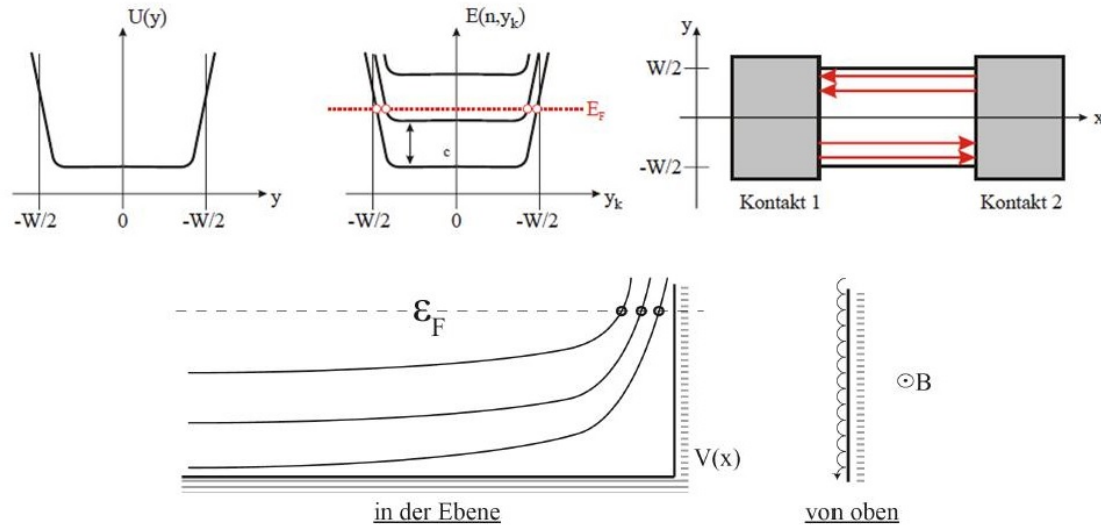


Fig. 2.42: Under the influence of the confining potential the Landau levels at the sample edge are modified, resulting in 1D states (so-called edge states) when the Fermi energy is crossed [top image: T. Klar, Praktikumsanleitung University of Giessen].

distances from the sample edge. These edge states lead to a net transport of electrons. The characteristic distance of the edge states from the edges can be estimated to $D_{ch} = \sqrt{(2\nu + 1) \frac{\hbar}{eB}}$ with $D_{ch} \ll W$. The simultaneous zeros in ρ_l and plateaus in ρ_H occur whenever the Fermi energy does not coincide with a Landau level, while maxima in ρ_l and transitions between plateaus occur whenever ϵ_F coincides with a Landau level.

Figure 2.43 shows an example of the longitudinal and transversal resistances in the quantum Hall effect measured in the Advanced Lab Course Nanotechnology in Tübingen. Plotting the longitudinal resistance in dependence of $1/B$ shows the periodicity of the oscillations in $1/B$. For lower magnetic fields, two spins are united within each oscillation, while for higher fields the spin degeneracy is increasingly lifted, and the oscillations split up. Plotting the inverse of the Hall resistance (the Hall conductance) over $1/B$ clearly displays the constant spacing of the plateaus in $1/B$, and the conductance as multiple integers of $2e^2/h$ for low magnetic fields, and of e^2/h for high magnetic fields when the two spin states are resolved.

More recent measurements of the quantum Hall effect in ultra-high mobility 2D electron gases at ultra-low temperatures demonstrate extended regions of exact conductance quantisation (cf. e.g. Fig. 2.44).

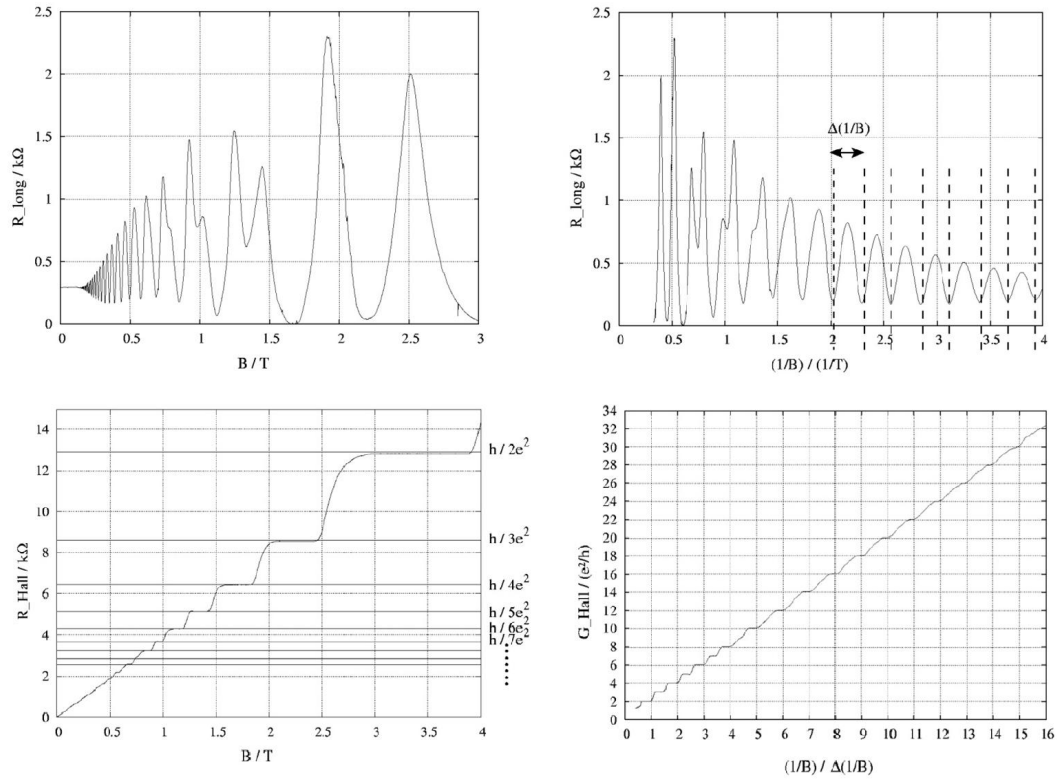


Fig. 2.43: Dependence of the longitudinal and the transversal Hall resistance on B and periodicity in $1/B$

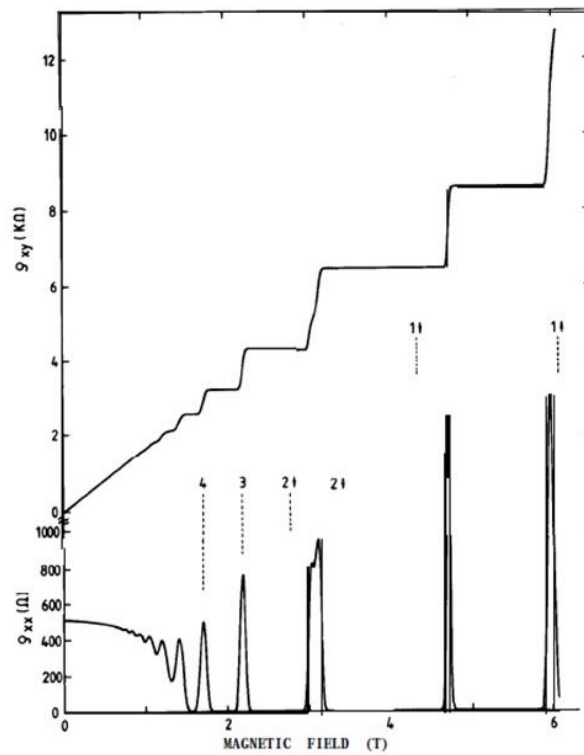


Fig. 2.44: Longitudinal and Hall resistance in a high mobility 2D electron gas

Fractional Quantum Hall Effect

The fractional quantum Hall effect was discovered in very high electron mobility systems and was rewarded by the Nobel Prize in physics for Laughlin, Störmer and Tsui in 1998. The observed phenomena are comparable to the quanten Hall effect, with zeros in the longitudinal resistance and plateaus in the transversal resistance when the Fermi energy does not coincide with a Landau level, however the plateaus appear at fractional multiples of $\frac{h}{e^2}$:

$$\rho_l \simeq 0 \quad \text{and} \quad \rho_H = \frac{h}{e^2} \frac{p}{q} \quad \text{with} \quad p, q \in \mathbb{N} \quad (2.73)$$

The reason can be found in so-called **composite fermions**, quasi-particles composed of defined numbers of electrons and flux quanta. The effective magnetic field experienced by a composite fermion is modified to $\vec{B}^* = \vec{B} \pm 2pn\phi_0$, with n the 2D particle density, $2p$ the number of vortices in the composite fermion, and $\phi_0 = \frac{h}{e}$ the composite fermion flux quantum. The fractional quantum Hall effect thus corresponds to an integer quantum Hall effect for composite fermions.

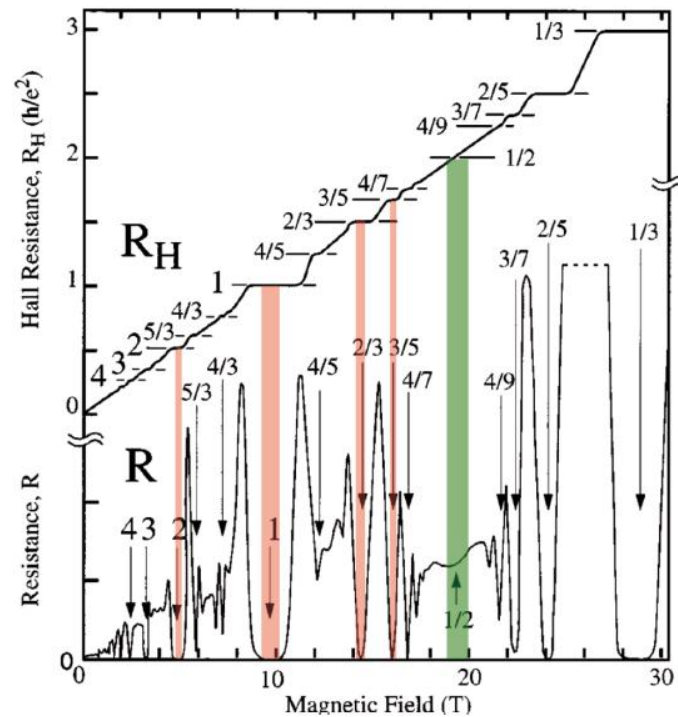


Fig. 2.45: Longitudinal and Hall resistance in the fractional quantum Hall effect

Quantum Hall Effect in graphene

Single monolayers of graphene as well as few-layer graphene exhibit a pronounced quantum Hall effect. In contrast to the 2D electron systems discussed so far however, for single layer graphene a quantisation in half-integer multiples of $4e^2/h$ is observed, while the Hall resistance for double layer graphene is quantised in integer multiples of $4e^2/h$. This effect will be briefly illustrated in the chapter “Carbon nanostructures”.

2.4.4 (Quasi-)1dim systems: quantum wires

Constraining the motion of electrons within the plane can lead to the formation of 1D or quasi-1D wires when the width of the defined channels becomes comparable to the Fermi wavelength λ_F . The properties of such channels show interesting phenomena, for the explanation of which it is also important to consider the scattering length scales.

The following three characteristic regimes can be distinguished:

- **Ballistic regime:** $l_\Phi \gg l_e \gg L, W$

In this regime the motion of charge carriers is dominated by the geometry of the confining wire, and specular reflection should occur along the length of the channel (Fig. 2.46). The conductance is dominated by the quantum-mechanical transmission of the modes propagating in the wire. This is the most appropriate regime for applying the Landauer theory (see below).

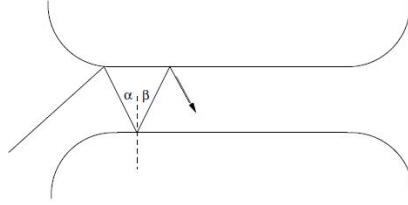


Fig. 2.46: Quantum wire in the ballistic regime, specular reflection at walls only

- **Quasi-ballistic regime:** $l_\Phi \gg L > l_e, W$

In this regime a small, finite number of scattering centres dominate the conductance characteristics. Phase coherent closed paths lead to interfering terms, and characteristic universal conductance fluctuations (UCF) are observed (Fig. 2.47): $\langle \Delta g \rangle \propto \frac{e^2}{\pi h}$. Such universal conductance fluctuations are found in metallic wires and demonstrate the non-locality of a conductance measurement as well as the incomplete averaging of interference terms in mesoscopic devices.

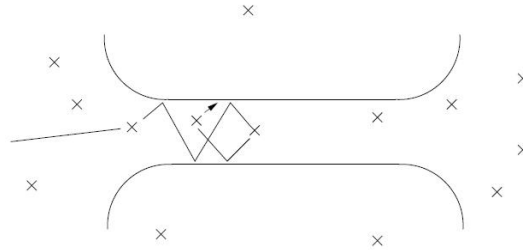


Fig. 2.47: Quantum wire in the quasi-ballistic regime, some impurity scattering

- **Diffusive regime:** $l_\Phi \gg L, W > l_e$

Strictly speaking this regime exists only in the quasi-1D limit where many modes in the channel are occupied (i.e. $W > \lambda_F$). The UCFs average to zero (Fig. 2.48).

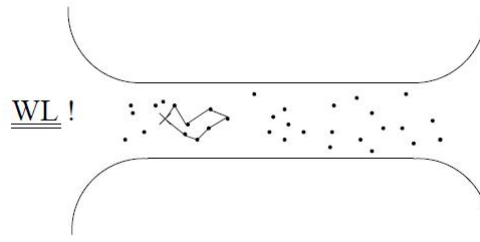


Fig. 2.48: Quantum wire in the diffusive regime, scattering dominates

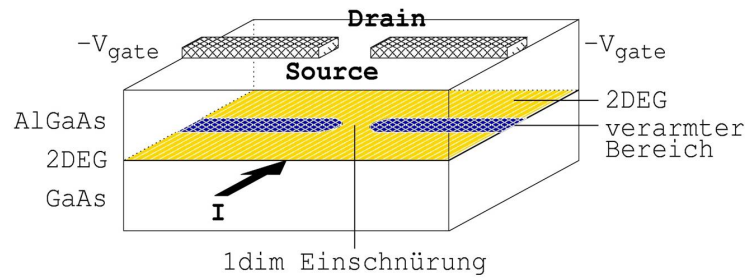


Fig. 2.49: Schematic of a quantum point-contact creating a (quasi-)1D channel in a 2D electron gas by applying a negative voltage to a split-gate

To create a (quasi-)1D quantum wire for experimental purposes, narrow constrictions can be introduced within a 2D electron gas, for example in a GaAs/AlGaAs heterostructure. Such so-called **quantum point-contacts** have tuneable widths and are interesting systems for fundamental studies. The schematic of an electrostatically induced quantum point-contact is outlined in Fig. 2.49. A pair of electrodes separated by a narrow gap, a so-called split-gate, is fabricated on top of a sample with a 2D electron gas buried a few 10 nm below the surface. When a negative gate voltage is applied to the electrodes, the electron gas below the electrodes is depleted and a potential wall

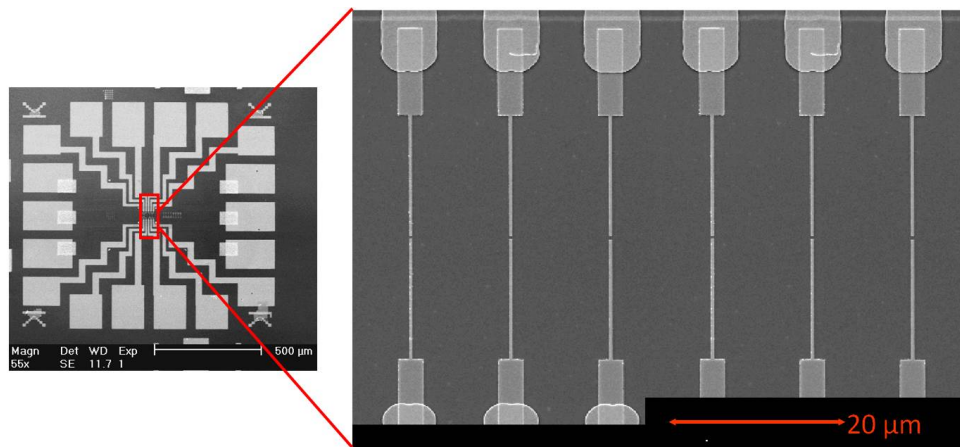


Fig. 2.50: SEM images of a mesa structure for transport measurements with a series of quantum point contacts defined at the center by electron beam lithography

is created below the gates. These areas, marked in blue, are no longer available for the transport of electrons through the 2D electron gas. Current flow only takes place through the (quasi-)1D constriction. In this channel, conductance quantisation takes place (see next section), and discrete modes are observed. The channel width, and thus the number of modes in the channel, can be varied via the gate voltage. When transport is restricted to a single mode, the wire corresponds to a true 1D system.

Figure 2.50 shows the scanning electron micrographs (SEM) of a series of such split-gate quantum point-contacts. The contacted mesa structure for the transport measurements is fabricated by optical lithography according to the fabrication steps shown in Fig. 2.34. In addition, electron beam lithography is performed at the center of the mesa to create the sub-micron sized split-gates as shown in the magnified SEM image on the right.

There are several other realisations of 1D quantum wires apart from this model system, such as e.g. vertical free-standing wires grown by chemical vapour deposition, but the electronic properties discussed in the following are comparable for different 1D systems.

Conductance and transmission in mesoscopic systems

Consider the transmission in a 1-dimensional ballistic conductor in the absence of any scattering. When no scattering occurs between the electronic states, the transmission may be regarded as perfect and the states propagate without decay of momentum. The current may be considered as a one-dimensional channel of nearly-free electrons (i.e. $m = m^*$), but otherwise parabolic in their dispersion: $\epsilon(k) = \frac{\hbar^2 k^2}{2m^*}$.

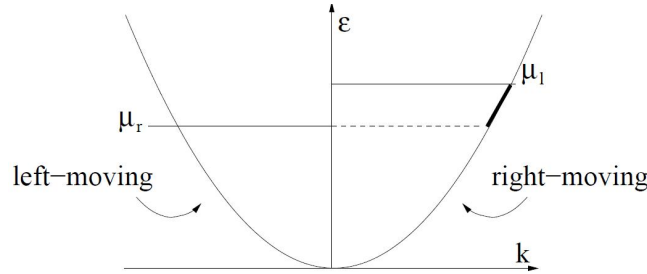


Fig. 2.51: Parabolic dispersion relation in one dimension

Assuming further that all right-moving states emanate from a reservoir with well-defined chemical potential μ_l and $k > 0$, the current may be calculated by considering only the states whose momentum has no equivalent occupied state in the other direction, i.e. the right-moving states with energy between μ_r and μ_l when $\mu_l > \mu_r$. This corresponds to a voltage difference $\mu_l - \mu_r = -e\Delta V$ between the two reservoirs. Thus

$$I = - \int_{\mu_r}^{\mu_l} g_{1D}(\epsilon) e v(\epsilon) d\epsilon \quad (2.74)$$

where $g_{1D}(\epsilon)$ is the 1D density of states, and $v(\epsilon)$ the velocity of the states. Quite generally (i.e. independent of the exact details of the dispersion) we may write:

$$v(\epsilon) = \frac{\hbar k}{m^*} = \frac{1}{\hbar} \left(\frac{\partial \epsilon}{\partial k} \right) \quad (2.75)$$

in the so-called semi-classical approximation for the dynamics of the quantum states. Furthermore, the density of states in 1D is best considered within the simple momentum space where the states are equally spaced with separation (π/L) with a spin-degeneracy of 2 assumed. Thus

$$g(\epsilon) = g(k) \frac{\partial k}{\partial \epsilon} = \frac{1}{\pi} \frac{dk}{d\epsilon} \quad (2.76)$$

Thus the expressions for the current and the conductance can be rewritten as

$$I = -\frac{e}{\pi \hbar} \int_{\mu_r}^{\mu_l} \frac{dk}{d\epsilon} \frac{d\epsilon}{dk} d\epsilon = \frac{e^2}{\pi \hbar} \Delta V \quad (2.77)$$

$$G = \frac{I}{\Delta V} = \frac{e^2}{\pi \hbar} = \frac{2e^2}{h} \quad (2.78)$$

The conductance G of a perfectly conducting 1D channel thus exhibits **conductance quantisation** in units of $\boxed{\frac{e^2}{h}}$, which plays a fundamental role in the conductance of mesoscopic devices.

In the above picture, transmission and conductance can be viewed as fundamentally connected with each other, and the above conductance is that for a perfectly transmitting channel. This formalism can be described in the four-terminal **Landauer-Büttiker formula**.

The 4-point geometry is the most commonly used configuration for measuring the resistance of a device (Fig. 2.52). Two terminals are contacted as current probes, and the other two are used for voltage measurements.

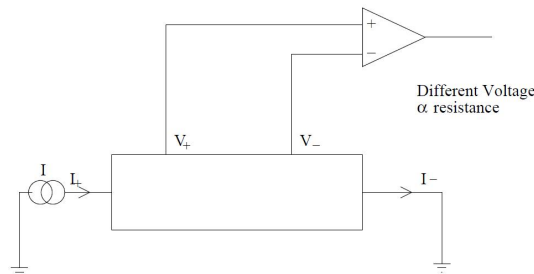


Fig. 2.52: 4-point geometry for conductance measurements

In such a geometry the 4-terminal formula can be used:

$$\frac{h}{2e} I_i = (N_i - R_{ii}) \mu_i - \sum_{j \neq i} T_{ij} \mu_j \quad (2.79)$$

where I_i is the current into the contact, N_i the number of channels involved in the transmission (channel $\hat{=}$ mode $\hat{=}$ 1D subband); R_{ii} the number of reflected channels; T_{ij} the number of transmitted channels (from $j \rightarrow i$) and μ_i the appropriate chemical potentials of the contacts.

For the geometry of a constriction as depicted in Fig. 2.53 (**quantum point contact (QPC)**, see previous section) with a defined small number of perfectly transmitting

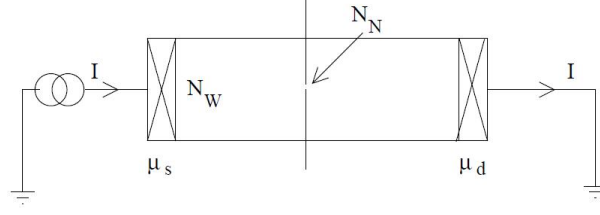


Fig. 2.53: Schematic of a 1D constriction in a transmission measurement

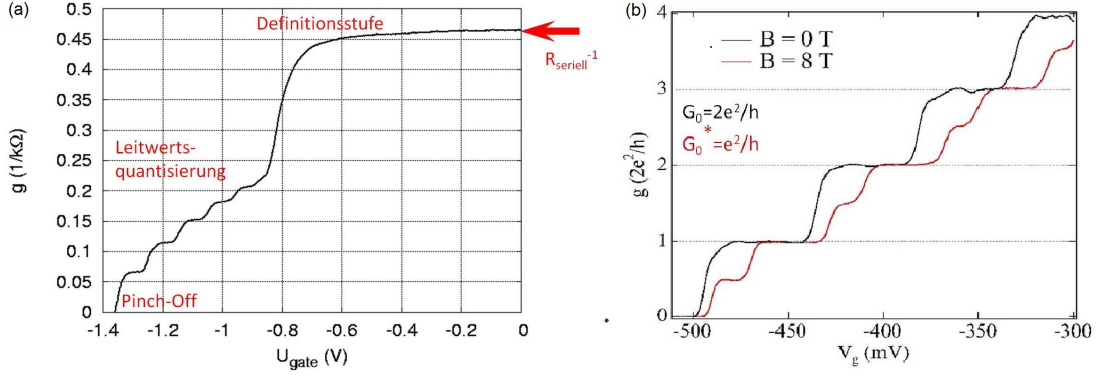


Fig. 2.54: Linear transport characteristics through a QPC: (a) Definition of the channel and successive depletion of the subbands by increasing $|V_g|$, (b) quantised conductance in spin-degenerate multiples of $2e^2/h$ for $B = 0$ T and spin-split units of e^2/h for $B > 0$ T [S. Cronenwett, PhD Thesis, Stanford University (2001)]

subbands N_N and $N_N \ll N_W$, where N_W is the number of channels in the wide region of the device, the equation can be directly solved:

$$\frac{h}{2e}I = (N_W - (N_W - N_N))\mu_s - N_N\mu_d = N_N(\mu_s - \mu_d) \quad (2.80)$$

$$\frac{eI}{\mu_s - \mu_d} = G = \frac{2e^2}{h}N_N \quad (2.81)$$

Thus the **conductance quantisation in 1D channels** is recovered.

Figure 2.54(a) depicts a typical conductance curve of a QPC when the negative gate voltage is increased. The measurements are performed at cryogenic temperatures such that the quantisation effects are not masked by thermal broadening. The transport measurements take place in the **linear regime**, i.e. very small source-drain-voltages V_{sd} are applied, therefore electrons contributing to the net current originate from a narrow window of energies $\mu_r < \epsilon < \mu_l$.

The conductance at $V_g = 0$ V is characteristic for the serial resistance of the measurement setup. When the negative gate voltage is increased, the conductance changes very little until the depletion in the underlying 2D electron gas is sufficient to define a 1D constriction (cf. Fig. 2.49). At the critical gate voltage, a *definition step* appears as a sudden drop of the conductance. Once the channel is defined, discrete 1D subbands evolve, and 1D conductance quantisation is observed in the shape of a distinct step-like series of plateaus, corresponding to a successive depletion of the subbands.

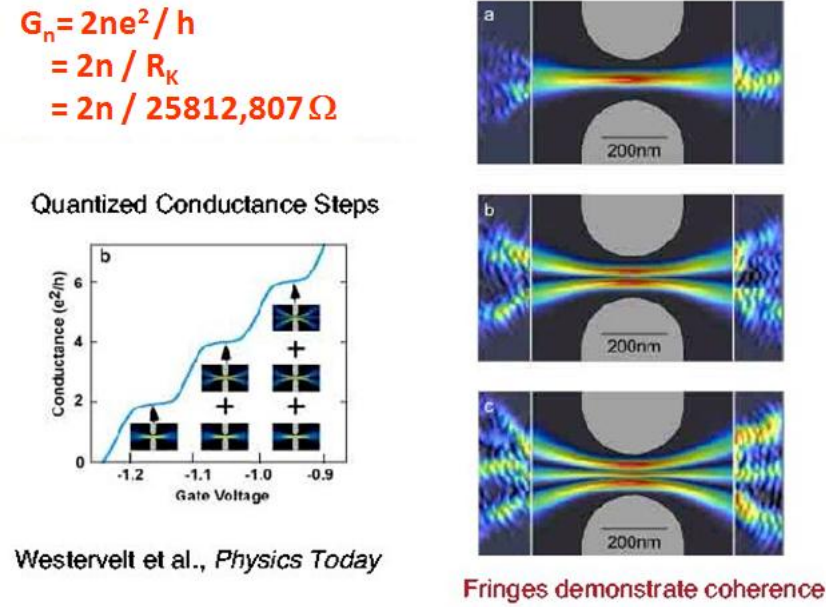


Fig. 2.55: Visualisation of the conducting modes in a QPC depending on the channel width. The electron flow is measured by local depletion via a scanning probe, and completed within the channel region by simulations [M.A. Topinka et al., *Physics Today* 56, 12 (2003)]

After the last mode is depleted, transport through the channel is no longer possible and the conductance drops to zero (*pinch-off*).

To recover the exact quantisation of the conductance as multiples of $\frac{2e^2}{h}$, the measured conductance needs to be corrected for the series resistance of the external circuit, as measured at $V_g = 0$ V. After this correction, clear spin-degenerate steps at multiples of $\frac{2e^2}{h}$ are observed, as seen in Fig. 2.54(b). If an additional magnetic field is applied, spin degeneracy is lifted, and conductance quantisation in units of $\frac{e^2}{h}$ becomes apparent.

The population of the different subbands was visualised by imaging the current flow through a QPC (see Fig. 2.55). A negatively charged cantilever tip is scanned over the surface, creating a local depletion region in the 2D electron gas below the tip. By measuring the position-dependent change in conductance, the current density is imaged. One can clearly see that different modes contribute to the transport depending on the number of conducting subbands.

Extending measurements to the **nonlinear regime**, another parameter can be added by varying the source-drain-voltage V_{sd} as well as the gate voltage V_g . By increasing $|V_{sd}|$, the “transport window” $\mu_l - \mu_r$ is increased as schematically shown in Fig. 2.56(a). While in the linear regime the number of left-moving and right-moving states is identical, in the nonlinear regime the number can differ depending on V_{sd} . In this simplified picture, for an odd difference between left- and right-moving states, plateaus of quantised conductance will appear at odd multiples of $\frac{e^2}{h}$, while for an even difference (including 0), plateaus occur at even multiples of $\frac{e^2}{h}$. The resulting nonlinear transport characteristics $G(V_{sd}, V_g)$ are depicted in the numerical simulation Fig. 2.56(b), where alternating series of conductance plateaus are observed.

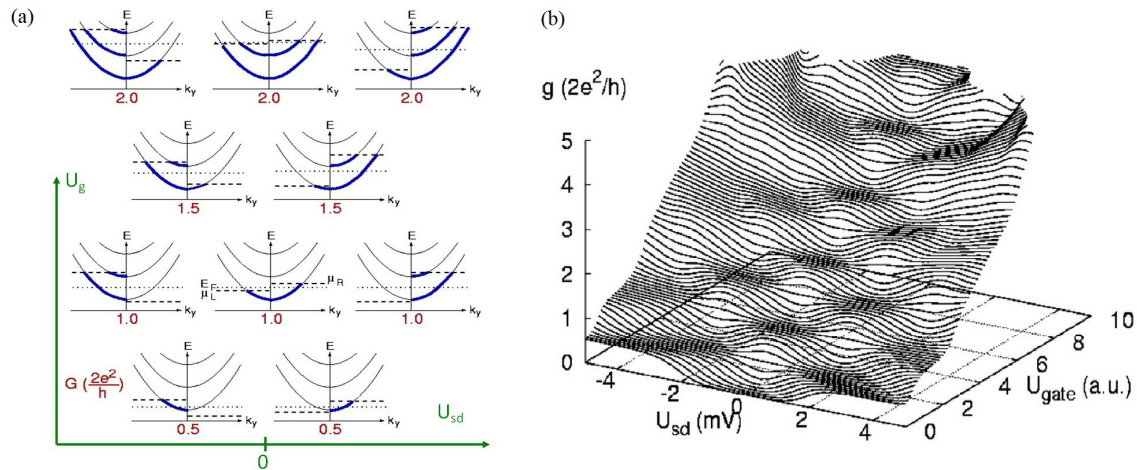


Fig. 2.56: Nonlinear transport through a QPC: (a) Schematic of the number of states contributing to transport through a QPC depending on the applied voltage V_{sd} , (b) numerical simulation of the conductance in nonlinear transport measurements depending on the applied source-drain- and gate voltage, exhibiting plateaus at even and odd multiples of e^2/h due to conductance quantisation [C. Höppler, PhD Thesis, University of Tuebingen (2004)]

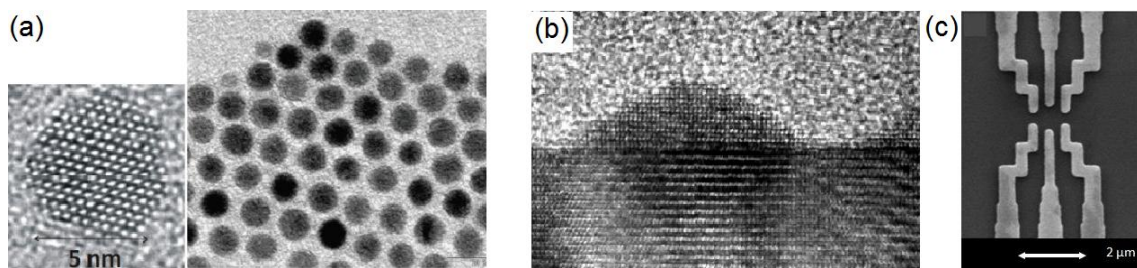


Fig. 2.57: Different realisations of quantum dots: (a) Transmission electron microscopy (TEM) image of nanocrystalline CdSe core-shell quantum dots [http://www.azoquantum.com], (b) TEM image of epitaxially grown GaN dots on AlN [http://www.ifp.tuwien.ac.at], (c) scanning electron microscopy (SEM) top-view of a quantum dot defined by three split-gates on top of a 2D electron gas

2.4.5 (Quasi-)0dim systems: quantum dots

Several different common realisations of quantum dots exist, which play important roles both in fundamental physics, studying the electronic transport and the optical properties of such “artificial atoms”, and in applications such as memory devices, quantum computers or photovoltaics:

- **Colloidal quantum dots:** Preparation via wet chemistry, or nanocrystal preparation by chemical vapour deposition. The individual dots exist separately as a powder or in solution. Typical sizes are on the order of \sim few to 50 nm, typical examples are III-V-semiconductors such as CdSe or CdTe, or core-shell-particles which are encapsulated in a stabilizing larger energy gap shell, such as Si/SiO₂ or CdSe/ZnS quantum dots (Fig. 2.57(a)).

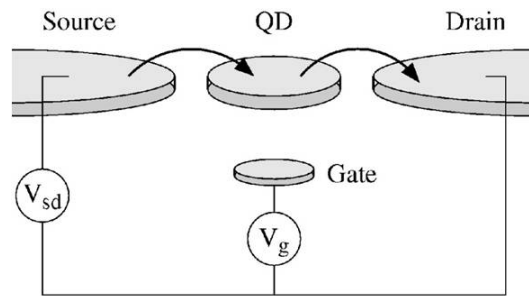


Fig. 2.58: Schematic of transport by successive electron tunneling through the tunneling barriers [L. Kouwenhoven et al., Kluwer (1997)]

- **Epitaxial quantum dots:** Due to stress and strain depending on a slight mismatch of the lattice constants, self-assembled quantum dots may form during epitaxial growth (e.g. MBE (molecular beam epitaxy)). Typical examples of such quantum dots are e.g. InAs dots within a GaAs matrix. The dots are laterally ordered in the same plane and have typically the shape of flat islands with diameters of \sim few 10 to few 100 nm and heights of \sim few to few tens of nm (Fig. 2.57(b)).
- **Electrostatically induced quantum dots:** Such tunable quantum dots may be prepared by lithographically structuring nano-electrodes, so-called split-gates, on top of a sample with a 2D electron gas buried at a depth of \sim 100 nm, e.g. in a GaAs/AlGaAs heterostructure. One such example is shown in Fig. 2.57(c). The three split-gates are employed to define an island with a discrete energy level system within the 2D electron gas, which is capacitively coupled to the electron reservoirs to both sides of the lateral split-gates via tunneling barriers. The central split gate can be used to shift the energy level system by applying a variable negative gate voltage. Similar quantum dots can be realized in lithographically confined silicon islands with applied gate electrodes. Due to the tunability of the key parameters such as the dot size, energy system, and coupling strengths, this type of quantum dot is widely used for basic physics studies.

The (quasi-)0D density of states of such quantum dots exhibits a discrete energy level system. Transport through a quantum dot is schematically shown in Figs. 2.58 and 2.59(a). The quantum dot corresponds to an isolated island, which is capacitively coupled to source and drain reservoirs via tunneling barriers. Electrons from the source reservoir can tunnel onto the dot as long as available states on the dot are present, and leave the dot by tunneling to the drain reservoir. The energy difference $\mu_s - \mu_d$ is defined by a source-drain-voltage V_{sd} . The discrete energy level system can be continuously shifted by capacitive coupling to an electrode to which a gate voltage V_g is applied.

Depending on the relative energies of the source, drain, and quantum dot levels, transport through the dot can be either blocked (*Coulomb blockade*) or allowed. The two situations are depicted in Fig. 2.59(a). When no discrete states are available for which $\mu_d \leq \epsilon_n \leq \mu_s$, the current $I = 0$ A. By shifting the energy levels via V_g , states can become available for tunneling onto and off the quantum dot, in which case a current $I > 0$ is observed. The energy gap between available states corresponds to

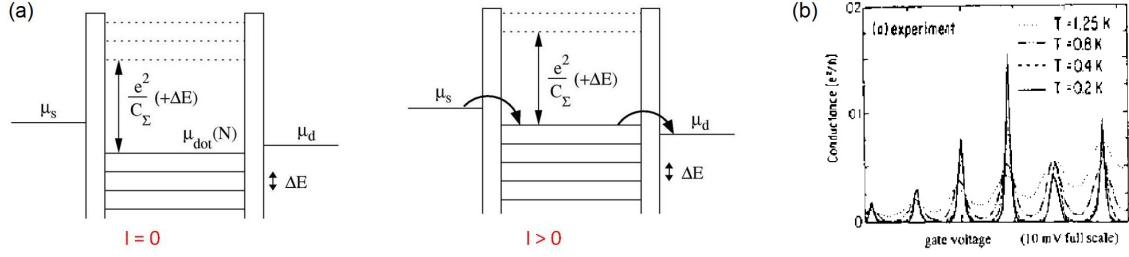


Fig. 2.59: Coulomb blockade: (a) schematic transport through a quantum dot, single electron tunneling is blocked or allowed depending on the gate voltage V_g , (b) resulting Coulomb blockade oscillations in the conductance $G(V_g)$ and their temperature dependence at $T = 200$ mK to 1.25 K [L. Kouwenhoven et al., Kluwer (1997)]

e^2/C_Σ , where C_Σ equals the sum of the capacitances between the dot, reservoirs and gate. Since each time an electron needs to leave the dot before a new electron can tunnel into the unoccupied state, **charge quantisation** is observed in the shape of **single electron transport**. Figure 2.59(b) illustrates the current flow or conductance through the quantum dot when V_g is continuously varied. Alternating zero conductance and **Coulomb blockade oscillations** are observed, which are correspondingly spaced at $\Delta V = e/C_\Sigma$. The width of the oscillation peaks depends critically on the temperature, therefore the experiments need to be performed at temperatures where $\frac{e^2}{C_\Sigma} > k_B T$. Figure 2.59(b) shows the broadening of the peaks when the temperature is increased from 200 mK to only 1.25 K. As in the case of quantum point contacts discussed before, the Coulomb blockade oscillations are measured in the **linear regime**. Only a very small source-drain-voltage V_{sd} is applied, such that either no level or a single level is found for which $\mu_d \leq \epsilon_n \leq \mu_s$.

By increasing and varying V_{sd} **nonlinear transport measurements** can be performed. The gate voltage regions in which transport is blocked are decreased for increasing V_{sd} , leading to characteristic **Coulomb diamonds** of voltages (V_{sd}, V_g) where the conductance is zero, as outlined in Fig. 2.60(a). When V_{sd} is increased further, several energy levels may fulfil the condition $\mu_d \leq \epsilon_n < \epsilon_{n+1} < \dots \leq \mu_s$ at the same time, leading to increased values of conductance, as also indicated in Fig. 2.60(a). Fig. 2.60(b) shows experimental proof of the Coulomb diamonds with $G(V_{sd}, V_g) = 0$.

Outlook: Optical properties of quantum dots

The *quantum confinement* induced by the nanoscale size of quantum dots leads to a splitting of the density of states into discrete energy levels as discussed above. The band gap of semiconductor quantum dots directly depends on the size of the quantum dot and increases with decreasing diameters, see Fig. 2.61. After excitation, quantum dots can act as bright emitters with a stable fluorescence. The wavelength of the emitted photons is defined by the optical band gap, thus the emission frequency can be tuned by the size of the quantum dot, with larger dots emitting in the red and smaller dots in the blue spectral range.

Quantum dots can be described as two-level systems and have been shown to undergo single-photon emission even at room temperature, making them attractive candidates

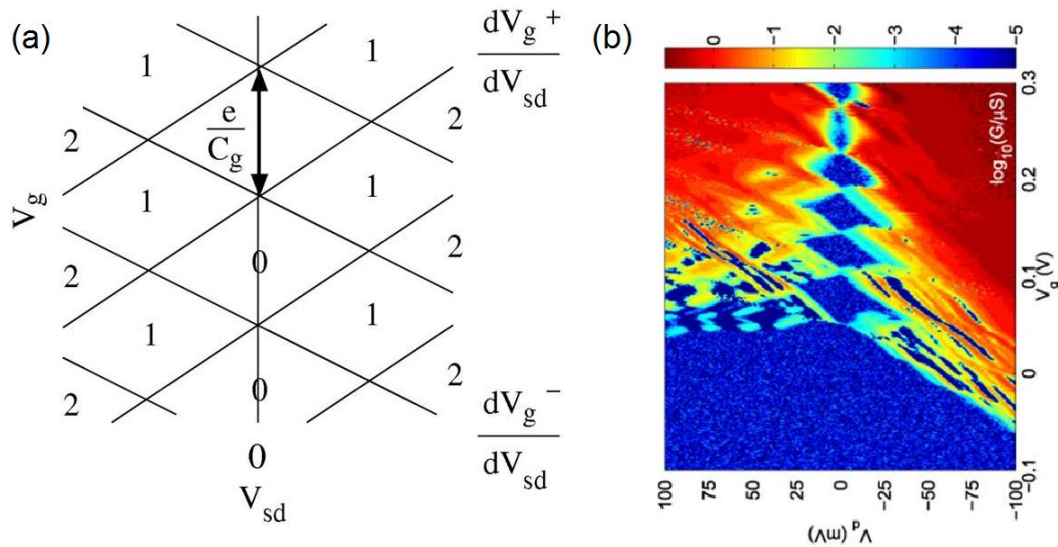


Fig. 2.60: Nonlinear transport characteristics of quantum dots: (a) schematic of the conductance through the quantum dot depending on the source-drain voltage V_{sd} and the gate voltage V_g , (b) measurement of the Coulomb diamonds (blue) characterising combinations of V_{sd} and V_g where transport through the dot is blocked [E. Prati et al., Nanotechnol. 23, 215204 (2012)]

for quantum technologies (see also ch. “Single-photon emitters”).

The **quantum yield** is defined as the ratio of the transition rate yielding an emission of photons compared to the overall transition rate:

$$QY = \frac{\gamma_r}{\gamma_r + \gamma_{nr}}, \quad (2.82)$$

with γ_r and γ_{nr} the radiative and non-radiative decay rate, respectively. The transition rate between initial and final states $\gamma_{i \rightarrow f}$ is determined by Fermi’s golden rule

$$\gamma_{i \rightarrow f} = \frac{2\pi}{\hbar} \rho(E_f) |V_{fi}|^2, \quad (2.83)$$

with $\rho(E_f)$ the density of states at the Fermi energy, and V_{fi} the transition matrix element of the perturbation.

Semiconductor quantum dots typically exhibit considerable trap states at their surface, which lead to a deterioration of the emission properties. In time traces of their intensity, a characteristic blinking behaviour is observed, with alternating intermittent on- and off-states. For this reason, they are often passivated by a larger band gap shell. The choice of band gap engineering leads to either type I or type II core/shell quantum dots depending on the relative positions of the conductance and valence band edges of the core and shell, cf. Fig. 2.62. Frequently used materials are e.g. CdSe, CdS, CdTe, ZnSe, or ZnS. Core/shell quantum dots are less sensitive to changes in the environment and more stable against photodegradation. They also enable an increased quantum yield due to the reduced number of trap states. The shell offers an additional degree of freedom for tuning the emission, and it can serve as a spacer material for binding the quantum dot to antenna structures or molecules to avoid quenching (a reduction of the emission due to an increase in non-radiative energy transfer processes).

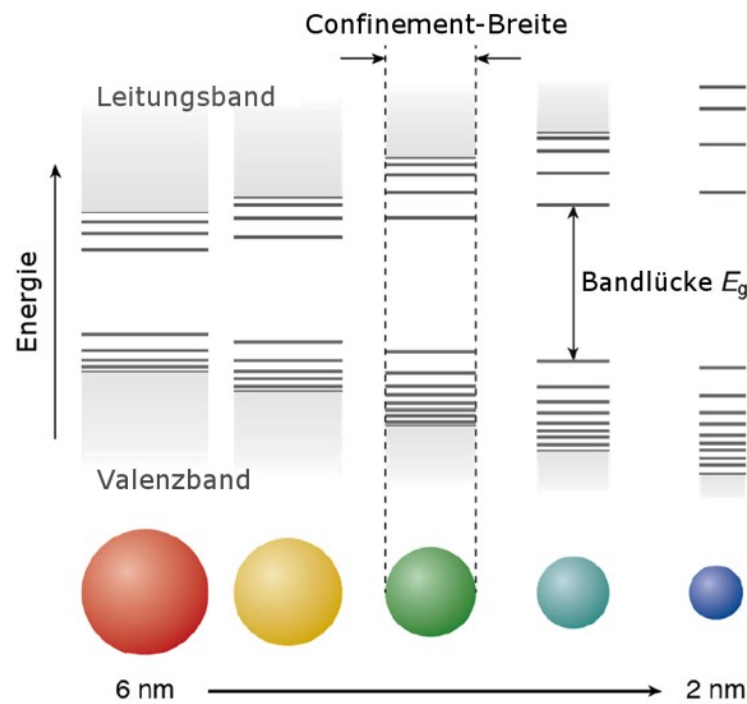


Fig. 2.61: Dependence of the band structure of quantum dots on their diameter [F.T. Rabouw et al., Topics in Current Chemistry 374(5), 58 (2016)]

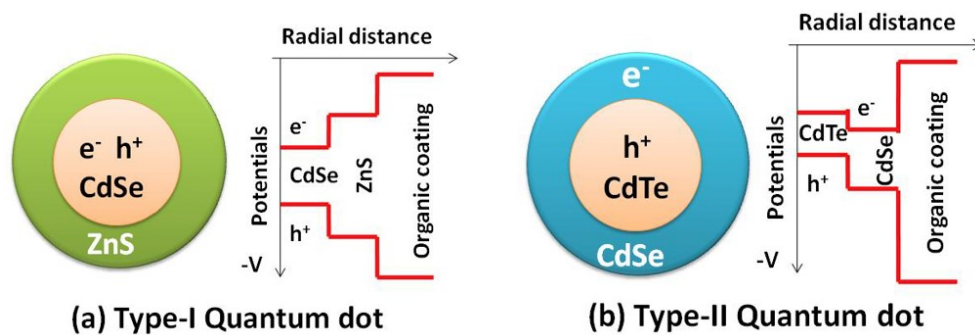


Fig. 2.62: (a) Type I and (b) type II quantum dots [K.E. Jasim, InTech (2015)]